arXiv:1103.3259v1 [cond-mat.supr-con] 16 Mar 2011

Pairing strength and symmetries of $(\mathrm{K,Tl})\mathrm{Fe}_x\mathrm{Se}_2$ in comparison with iron pnictides

Rong Yu,[1,*] Pallab Goswami,[1,*] Qimiao Si,[1] Predrag Nikolic,[2] and Jian-Xin Zhu[3]

[1]*Department of Physics and Astronomy, Rice University, Houston, TX 77005*
[2]*Department of Physics and Astronomy, George Mason University, Fairfax, VA 22030*
[3]*Theoretical Division, Los Alamos National Laboratory, Los Alamos, NM 87545*

We address singlet pairing states in the newly discovered superconducting iron selenides $(\mathrm{K,Tl})\mathrm{Fe}_x\mathrm{Se}_2$ within an incipient Mott approach. We analyze a five orbital t-J_1-J_2 model, and contrast the results with those of a related model for the iron pnictides. Similar to the pnictides case, an A_{1g} $s_{x^2y^2}$ state and a B_{1g} $d_{x^2-y^2}$ state are quasi-degenerate in the $\mathrm{J}_1 \sim \mathrm{J}_2$ magnetic frustration regime. In contrast to the pnictides case, an A_{1g} $s_{x^2+y^2}$ state is not competitive in the relevant parameter regime. The dominant pairing channels are fully gapped. The pairing amplitudes are of the same order as their pnictides counterparts, making it natural that the maximum T_c is comparable in the two systems.

Introduction: An important characteristic of iron-based superconductors is their large materials phase space. Comparing the properties of the different materials families promise to shed considerable light on the physics of these systems. A major development along this direction is the very recent discovery of high temperature superconductivity in a new family of iron chalcogenides $\mathrm{KFe}_x\mathrm{Se}_2$ [1] and $(\mathrm{K,Tl})\mathrm{Fe}_x\mathrm{Se}_2$ [2]. These and related compounds [3, 4] have a maximal $\mathrm{T}_c \sim 30K$, which is comparable to that of 122 iron pnictides such as the doped $\mathrm{BaFe}_2\mathrm{As}_2$. Importantly, both the angle resolved photoemission experiments [5–7] and *ab initio* band structure calculations using local-density approximation (LDA) [8–11] show that the fermiology of the new chalcogenides in the normal state is dramatically different from that in iron pnictides. In contrast to the pnictides where both electron and hole pockets are present respectively at M and Γ points of the extended Brillouin zone, only electron pockets are present in the new chalcogenides. Equally important, the discovery has added a new twist to the consideration regarding the strength of the electronic correlations in the iron based superconductors. Similar to the iron pnictides, superconductivity occurs near an antiferromagnetically ordered phase. However in contrast to the pnictides where the antiferromagnetic phase is a semi-metal, the antiferromagnetic phase in the new iron chalcogenides is an insulator [2, 12]. The observation of an insulating state and the emergence of antiferromagnetic order with large moment [13] in the absence of quasi-nested electron and hole pockets certainly point towards the importance of correlation effects. It may be that the parent compounds of the new materials are Mott insulators, as suggested by microscopic model calculations [14, 15] that incorporate the band-narrowing effect seen in LDA studies [10, 16].

Ever since the discovery of the high temperature superconductivity in iron pnictides, the strength of the electronic correlation has been the subject of debate. Both weak and strong coupling pictures had partial success in explaining the $(\pi, 0)$ magnetic order in the parent compounds, and the emergence of a sign changing A_{1g} state as the dominant pairing channel. In the parent iron pnictides, a large electrical resistivity (“bad metal”), a strong suppression of Drude weight [17], as well as the temperature-induced spectral weight transfer [18–20] suggest significant correlation effects. These properties have been interpreted in terms of a proximity to a putative Mott transition [21–23]. Interestingly the room temperature electrical resistivity of the new iron chalcogenides is several orders of magnitude larger than that of pnictides, and with decreasing temperature the resistivity shows exponential enhancement [2, 12]. Strong correlation effects are also observed in the suppression of the low frequency optical conductivity [24]. All these support the notion that both the parent iron selenides and parent iron pnictides are in the vicinity (but on two different sides) of the Mott transition. They make it important to understand the superconducting pairing in these materials from a strong coupling perspective [21–23, 25–29].

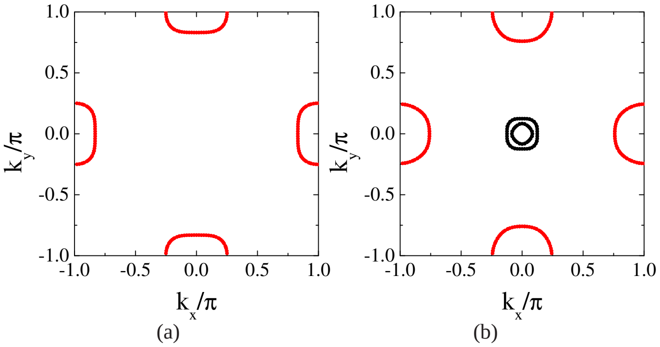

(a) (b)

FIG. 1. (Color online) The contrasting Fermi surfaces of (a) $\mathrm{KFe}_x\mathrm{Se}_2$, and (b) iron pnictides, in the extended Brillouin zone corresponding to one iron per unit cell, as obtained by using a five orbital tight binding model, for electron doping $\delta = 0.15$. There are only electron pockets at M points $(\pm\pi, 0)$ and $(0, \pm\pi)$ for $\mathrm{KFe}_x\mathrm{Se}_2$. For iron pnictides, there are in addition two hole pockets at the Γ point $(0, 0)$.

Several experimental results have especially motivated our study. The comparable maximum T_c observed in the $(\mathrm{K,Tl})\mathrm{Fe}_x\mathrm{Se}_2$ compounds and their 122 pnictides counterpart suggest some degree of commonality in the underlying mechanism for superconductivity. At the same time, even though the pairing symmetry remains to be determined, nearly all experiments have pointed towards a fully gapped superconductivity. This is in strong contrast to the iron pnictides, in which both nodeless and nodal features have been seen in different materials families or even at different dopings of a same family. Our results will shed light on such similarities and differences. We note that weak coupling approaches, based on functional renormalization group [30, 31] and spin-fluctuation exchange RPA [32, 33], have led to a dominant instability in the B_{1g} $\mathrm{d}_{x^2-y^2}$ pairing channel due to the repulsive inter-electron-pocket pair scattering. Our work is closer in spirit to the strong-coupling approach to the $(\mathrm{K},\mathrm{Tl})\mathrm{Fe}_x\mathrm{Se}_2$ systems [14, 15], although the pairing strength and aforementioned similarities and differences compared to the iron pnictides have not been studied.

Five-orbital Model: Our multi-orbital t-J_1-J_2 Hamiltonian [21, 22, 25, 27] is given by

$$\begin{aligned} H = &- \sum_{i<j,\alpha,\beta,s} t_{ij}^{\alpha\beta} c_{i\alpha s}^{\dagger} c_{j\beta s} + h.c. - \mu \sum_{i,\alpha} n_{i\alpha} \\ &+ \sum_{\langle ij\rangle,\alpha,\beta} J_1^{\alpha\beta} \left(\vec{S}_{i\alpha} \cdot \vec{S}_{j\beta} - \frac{1}{4} n_{i\alpha} n_{j\beta} \right) \\ &+ \sum_{\langle\langle ij\rangle\rangle,\alpha,\beta} J_2^{\alpha\beta} \left(\vec{S}_{i\alpha} \cdot \vec{S}_{j\beta} - \frac{1}{4} n_{i\alpha} n_{j\beta} \right), \end{aligned} \tag{1}$$

where $c_{i\alpha s}^{\dagger}$ creates an electron at site i, with orbital index α and spin projection s; μ is the chemical potential and $t_{ij}^{\alpha\beta}$ the hopping matrix. The orbital index $\alpha = 1, 2, 3, 4, 5$ respectively correspond to five 3d orbitals $3\mathrm{d}_{xz}$, $3\mathrm{d}_{yz}$, $3\mathrm{d}_{x^2-y^2}$, $3\mathrm{d}_{xy}$, and $3\mathrm{d}_{3z^2-r^2}$ of iron. The nearest-neighbor (n.n., $\langle ij\rangle$) and next-nearest-neighbor (n.n.n., $\langle\langle ij\rangle\rangle$) exchange interactions are respectively denoted by $J_1^{\alpha\beta}$ and $J_2^{\alpha\beta}$. The spin operator $\vec{S}_{i\alpha} = \frac{1}{2}\sum_{s,s'} c_{i\alpha s}^{\dagger} \vec{\sigma}_{ss'} c_{i\alpha s'}$ and the density operator $n_{i\alpha} = \sum_s c_{i\alpha s}^{\dagger} c_{i\alpha s}$, with $\vec{\sigma}$ representing the Pauli matrices. The double-occupancy prohibiting constraint from the fermion is implicitly incorporated by the renormalization of the dispersion. As discussed at length in the Supplementary Material [34], the phase diagram is insensitive to this when the exchange interactions are measured w.r.t. the renormalized band dispersion. In a previous study of a multi-orbital t-J_1-J_2 model for iron pnictides [27], it has been demonstrated by three of the present authors that the dominant pairing symmetry is governed by the intra-orbital exchange interactions, and the consideration of the orbitally off-diagonal exchange interaction only introduces quantitative modifications of the phase diagram. Therefore to keep the analysis simple, we will consider the orbitally diagonal exchange couplings $J_1^{\alpha\beta} = \mathrm{J}_1\delta_{\alpha\beta}$ and $J_2^{\alpha\beta} = \mathrm{J}_2\delta_{\alpha\beta}$. Experiments have suggested that the ordering of the Fe-site vacancies goes away in some superconducting materials [2, 35, 36], but not in others [2, 13]. For simplicity, we will consider here the case with the 122 tetragonal symmetry.

To describe the fermiology, we use a tetragonal symmetry preserving tight binding model, involving all five 3d orbitals of iron. In the momentum space the 5×5 tight-binding matrix, and its eigenvalues will be respectively denoted by $\hat{\xi}_k$, and $E_{j,\mathbf{k}}$. The total number of electrons is determined by the chemical potential and the dispersion relations, according to $n = 2\sum_{j,\mathbf{k}} \theta(\mu - E_{j,\mathbf{k}})$, and carrier doping $\delta = |n - 6|$. The tight-binding parameters are fixed by fitting the band structure obtained from the LDA calculation. The details of the tight-binding parametrization for iron chalcogenides and the associated band dispersions are discussed in the Supplementary Material [34]. For $(\mathrm{K},\mathrm{Tl})\mathrm{Fe}_x\mathrm{Se}_2$ the band dispersions correctly produce the electron pockets near the M points, as illustrated in Fig. 1(a) for $\mathrm{KFe}_x\mathrm{Se}_2$. The electron and hole like Fermi pockets obtained from a similar five orbital tight-binding model of iron pnictides are shown in Fig. 1(b), to contrast the fermiology of the two materials. In the Supplementary Material [34] we show the fermiology of $\mathrm{TlFe}_x\mathrm{Se}_2$, which again consists of only electron pockets. We note that photoemission experiments [5–7] have suggested that very weak electron-like pockets also exist near the Γ point; unlike their hole counterpart in the pnictides, these electron pockets have very small spectral weight and are not expected to play an important role in driving superconductivity.

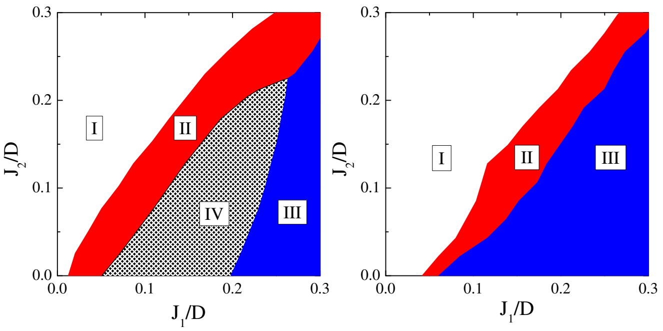

(a) (b)

FIG. 2. (Color online) Zero temperature phase diagrams of (a) $\mathrm{KFe}_x\mathrm{Se}_2$ and (b) iron pnictides, for electron doping $\delta = 0.15$. Region I corresponds to A_{1g} state with dominant $s_{x^2y^2}$ channel. Regions II and III mark an $\mathrm{A}_{1g} + i\mathrm{B}_{1g}$ state with dominant $s_{x^2y^2}$ and $d_{x^2-y^2}$ channels (II) and dominant $s_{x^2+y^2}$ and $d_{x^2-y^2}$ channels (III); the phase locking occurs only at low temperatures. Region IV for $\mathrm{KFe}_x\mathrm{Se}_2$ is a pure B_{1g} state with dominant $d_{x^2-y^2}$ channel.

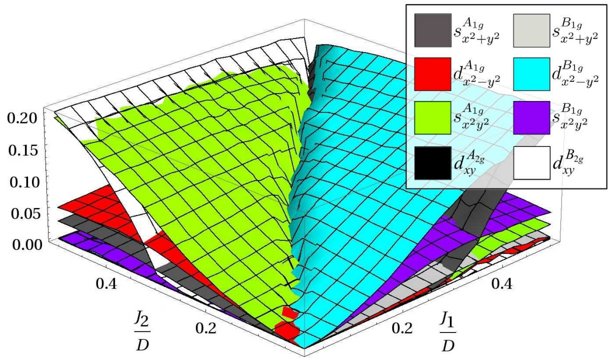

FIG. 3. (Color online) The pairing amplitudes for xz/yz orbitals of $\mathrm{KFe}_x\mathrm{Se}_2$ for electron doping $\delta = 0.15$. In the J_2 dominated regimes, for $\mathrm{J}_2/\mathrm{D} \leq 0.3$, A_{1g} $s_{x^2y^2}$ is the strongest pairing channel. In the likewise J_1 dominated regime, this is the B_{1g} $d_{x^2-y^2}$ channel.

Degenerate spin singlet pairing states in the absence of kinetic energy: The spin singlet, intraorbital pairing operators are defined as $\Delta_{\mathbf{e},\alpha\alpha} = \langle c_{i\alpha\uparrow}c_{i+\mathbf{e}\alpha\downarrow} - c_{i\alpha\downarrow}c_{i+\mathbf{e}\alpha\uparrow}\rangle/2$, where $\mathbf{e} = \hat{x}, \hat{y}, \hat{x}\pm\hat{y}$. Two types of pairing states $\Delta_{\hat{x},\alpha} = \pm\Delta_{\hat{y},\alpha}$, respectively denoted as $s_{x^2+y^2}$ and $d_{x^2-y^2}$ states with momentum space form factors $g_{x^2+y^2,\mathbf{k}} = \cos k_x + \cos k_y$, $g_{x^2-y^2,\mathbf{k}} = \cos k_x - \cos k_y$ arise due to the nearest neighbor exchange interaction, and they are energetically degenerate in the absence of kinetic energy. Similarly the next nearest neighbor exchange gives rise to two degenerate pairing states $\Delta_{\hat{x}+\hat{y},\alpha} = \pm\Delta_{\hat{x}-\hat{y},\alpha}$, respectively denoted as $s_{x^2y^2}$ and d_{xy} states, with momentum space form factors $g_{x^2y^2,\mathbf{k}} = \cos(k_x - k_y) + \cos(k_x + k_y)$, $g_{xy,\mathbf{k}} = \cos(k_x - k_y) + \cos(k_x + k_y)$. A strong magnetic frustration, characterized by $J_1 \sim J_2$, leads to an enhanced degeneracy among the four paired states.

Degeneracy lifting effects of the kinetic energy: The kinetic energy term lifts most of these degeneracies and in the strong frustration regime leaves a quasi-degeneracy among a reduced set of pairing states. To study the full problem we perform a mean-field decoupling [25, 27, 37] of the exchange interaction terms. We introduce four complex singlet pairing amplitudes for each orbitals, and write the following 5×5 pairing matrix $\mathbf{\Delta}_{\mathbf{k}} = \sum_a \mathrm{diag}[\Delta^a_{\mathbf{k},11}, \Delta^a_{\mathbf{k},22}, \Delta^a_{\mathbf{k},33}, \Delta^a_{\mathbf{k},44}, \Delta^a_{\mathbf{k},55}]$, where $\Delta^a_{\mathbf{k},\alpha\alpha} = \Delta^a_{\alpha\alpha} g_{a,\mathbf{k}}$, and the index a corresponds to $s_{x^2+y^2}$, $d_{x^2-y^2}$, $s_{x^2y^2}$ and d_{xy} symmetries. In the subspace of xz and yz 3d-electron-orbitals, which transform as a doublet under the tetragonal point group operations, there are the following four classes of intra-orbital pairing states for an orbitally diagonal J$_1$-J$_2$ model: (i) A_{1g} : $[s^{A_{1g}}_{x^2+y^2} g_{x^2+y^2,\mathbf{k}} + s^{A_{1g}}_{x^2y^2} g_{x^2y^2,\mathbf{k}}]\tau_0 + d^{A_{1g}}_{x^2-y^2} g_{x^2-y^2,\mathbf{k}}\tau_z$; (ii) B_{1g} : $d^{B_{1g}}_{x^2-y^2} g_{x^2-y^2,\mathbf{k}}\tau_0 + [s^{B_{1g}}_{x^2+y^2} g_{x^2+y^2,\mathbf{k}} + s^{B_{1g}}_{x^2y^2} g_{x^2y^2,\mathbf{k}}]\tau_z$; (iii) A_{2g} : $d^{A_{2g}}_{xy} g_{xy,\mathbf{k}}\tau_z$; and (iv) B_{2g} : $d^{B_{2g}}_{xy} g_{xy,\mathbf{k}}\tau_0$. Here τ_0 and τ_z are the Pauli matrices in the two-orbital subspace. The eight pairing amplitudes $s^{A_{1g}}_{x^2+y^2}$ etc. are obtained as linear combinations of Δ^a_{11} and Δ^a_{22}, which are in turn linear combinations of $\Delta_{\mathbf{e},11}$, and $\Delta_{\mathbf{e},22}$.

Pairing phase diagram: We determine the pairing gap matrix by minimizing the ground state energy density

$$f = \sum_{\mathbf{e},\alpha} \frac{J_{\mathbf{e}}}{2} |\Delta_{\mathbf{e},\alpha\alpha}|^2 - \sum_{\mathbf{k},j} (\mathcal{E}_{\mathbf{k},j} - E_{\mathbf{k},j} + \mu), \qquad (2)$$

with respect to *all* $\Delta_{\mathbf{e},\alpha\alpha}$, where $\pm\mathcal{E}_{\mathbf{k},j}$ are the eigenvalues of the mean-field Hamiltonian

$$H_{mf} = \sum_{\mathbf{k}} \Psi^{\dagger}_{\mathbf{k}} \begin{bmatrix} \hat{\xi}_{\mathbf{k}} - \mu \mathbb{1}_{5\times5} & \mathbf{\Delta}_{\mathbf{k}} \\ \mathbf{\Delta}^{*}_{\mathbf{k}} & -\hat{\xi}_{\mathbf{k}} + \mu \mathbb{1}_{5\times5} \end{bmatrix} \Psi_{\mathbf{k}}, \qquad (3)$$

and $\Psi^{\dagger}_{\mathbf{k}} = (c^{\dagger}_{\mathbf{k}\alpha\uparrow}, c_{-\mathbf{k}\alpha\downarrow})$ is the ten-component Nambu spinor. Our calculations are performed in a canonical ensemble for a fixed doping or electron density. The grand canonical results for the phase diagram are qualitatively similar to the canonical ensemble results.

We show two illustrative zero temperature phase diagrams in Fig. 2(a) and Fig. 2(b) respectively for $\mathrm{KFe}_x\mathrm{Se}_2$ and iron pnictides, with an electron doping $\delta = 0.15$ ($n = 6.15$). The phase diagrams are shown for $0 \leq \mathrm{J}_1, \mathrm{J}_2 \leq 0.3D$, where D is the band width. The phase diagram in Fig. 2(a) is separated into four regions I, II, III, and IV, whereas that in Fig. 2(b) is separated into three regions I, II, and III. In the J$_2$ dominated region I, a pure A_{1g} state occurs with $s_{x^2y^2}$ being the dominant component. For iron pnictides this state corresponds to the $s_{\pm}$ state, that changes sign between electron and hole pockets. Close to the $\mathrm{J}_1 \sim \mathrm{J}_2$ magnetic frustration regime, the A_{1g} $s_{x^2y^2}$ and B_{1g} $d_{x^2-y^2}$ states are quasi-degenerate. In region II, due to this quasi-degeneracy between two types of pairing symmetries which follow different crystallographic representations, the lowest energy paired state is a time reversal symmetry breaking $\mathrm{A}_{1g} + i\mathrm{B}_{1g}$ state. In the J$_1$ dominated regime III, the paired state is again a time reversal-symmetry breaking $\mathrm{A}_{1g} + i\mathrm{B}_{1g}$ state, but the dominant components are A_{1g} $s_{x^2+y^2}$, and B_{1g} $d_{x^2-y^2}$ pairings. Note that there is only a crossover between regions II and III, and time-reversal symmetry breaking is expected only at very low temperatures. In the phase diagram of Fig. 2(a) for $\mathrm{KFe}_x\mathrm{Se}_2$, the additional region IV is dominated by J_1, but in this region a pure B_{1g} $\mathrm{d}_{x^2-y^2}$ state occurs. Notice that this pure B_{1g} phase is absent for iron pnictides. To illustrate the robustness and applicabil-

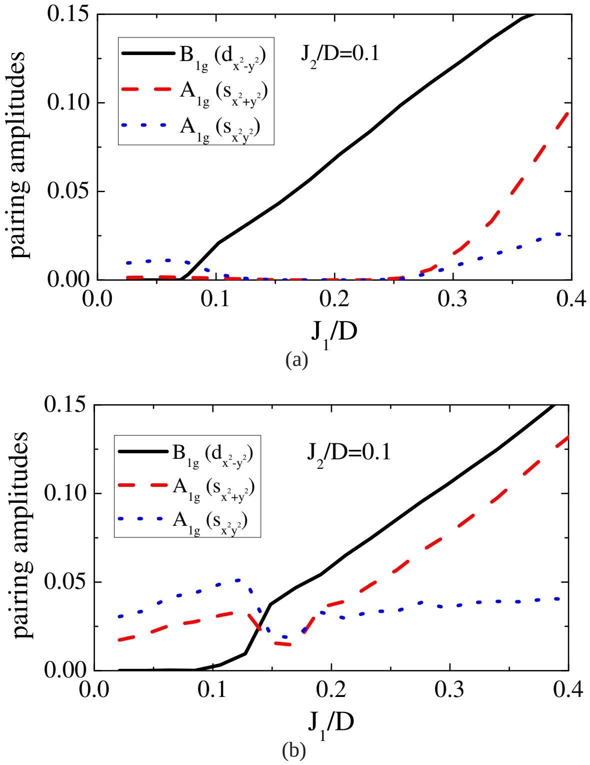

(a)

(b)

FIG. 4. (Color online) Comparison of the competing dominant pairing amplitudes A_{1g} $s_{x^2y^2}$, A_{1g} $s_{x^2+y^2}$, B_{1g} $d_{x^2-y^2}$ for xz/yz orbitals of (a) $\mathrm{KFe}_x\mathrm{Se}_2$ and (b) iron pnictides, both for electron doping $\delta = 0.15$. For $\mathrm{KFe}_x\mathrm{Se}_2$, the amplitude for the A_{1g} $s_{x^2+y^2}$ channel is strongly suppressed compared to the pnictides case. Correspondingly, a pure B_{1g} $d_{x^2-y^2}$ state is observed for $\mathrm{KFe}_x\mathrm{Se}_2$ but is absent in iron pnictides.

ity of the phase diagram Fig. 2(a) for $\mathrm{KFe}_x\mathrm{Se}_2$, we show a qualitatively similar phase diagram for $\mathrm{TlFe}_x\mathrm{Se}_2$ in the Supplementary Material [34].

To get an overall picture of the pairing strength, we show in Fig. 3 a three dimensional plot of the pairing amplitudes for xz/yz 3d-electron-orbitals of $\mathrm{KFe}_x\mathrm{Se}_2$. The other three d-orbitals may also contain significant pairing strength, depending on their spectral weight on the Fermi pockets (see [34] for details). Similar results for iron pnictides are also shown in the Supplementary Material [34]. The competition among the dominant pairing channels can be clearly observed in Fig. 4(a) and Fig. 4(b) respectively for $(\mathrm{K,Tl})\mathrm{Fe}_x\mathrm{Se}_2$ and iron pnictides. In these figures we show the dominant pairing amplitudes as a function of J_1/D, for a fixed value of $J_2/D = 0.1$. In Fig. 4(b), we notice, apart from the absence of pure B_{1g} phase, that A_{1g} $\mathrm{s}_{x^2+y^2}$ state has a significant contribution in the entire regime $0 \leq \mathrm{J}_1 \leq 0.4D$. This is important to understanding the nodeless vs. nodal gaps in the A_{1g} state of iron pnictides. This pairing state by itself will have nodes on the electron pocket, and for $\mathrm{KFe}_x\mathrm{Se}_2$ it is never very competitive in the weak to moderate J_1 regime. Corresponding pairing amplitudes of $\mathrm{TlFe}_x\mathrm{Se}_2$ are shown in the Supplementary Material [34].

The role of the fermiology behind the emergence of the dominant pairing states can be understood by considering the strength of the pairing kernels for different channels. Due to the smallness of d_{xy} form factor $\sin k_x \sin k_y$, in the vicinity of M and Γ points, the d_{xy} pairing kernel is very small for a set of small Fermi pockets, relevant to the iron based superconductors. For $(\mathrm{K,Tl})\mathrm{Fe}_x\mathrm{Se}_2$, which only possess small electron pockets at M points, the pairing kernel for $\mathrm{s}_{x^2+y^2}$ is also very small. In contrast both $\mathrm{d}_{x^2-y^2}$ and $\mathrm{s}_{x^2y^2}$ pairing kernels are much bigger around the M points, and in the weak to moderate (J_1,J_2) regime, these two states emerge as the dominant pairing states. For iron pnictides there are two small hole pockets around Γ point, and due to these pockets $\mathrm{s}_{x^2y^2}$ kernel becomes larger than $\mathrm{d}_{x^2-y^2}$, and $\mathrm{s}_{x^2y^2}$ dominates the larger portion of the phase diagram. Again due to the presence of the hole pockets $\mathrm{s}_{x^2+y^2}$ has a stronger competition with $\mathrm{d}_{x^2-y^2}$ state in pnictides.

Experimental implications: For $(\mathrm{K,Tl})\mathrm{Fe}_x\mathrm{Se}_2$, our calculations lead to dominating A_{1g} $\mathrm{s}_{x^2y^2}$ and B_{1g} $\mathrm{d}_{x^2-y^2}$ states in competition. Since both have nearly isotropic and nodeless gaps on the electron pockets, our results are consistent with existing experiments. For iron pnictides, the dominance of A_{1g} $\mathrm{s}_{x^2y^2}$ state in a large portion of the phase diagram is consistent with the expected $s_\pm$ paired state predicted by both weak and strong coupling approaches. The sizable contribution from $\mathrm{s}_{x^2+y^2}$ channel to A_{1g} state is important to understanding a possible strong momentum dependence or gap nodes of the A_{1g} state on the electron pockets in different pnictides compounds.

At the same time, our calculation shows similar pairing amplitudes for the two systems, thereby giving a natural understanding for the comparable transition temperatures.

At present there is no experimental estimation of the exchange couplings in the paramagnetic normal state. Future inelastic neutron scattering experiments should provide guidance in such a direction, and this will be important for understanding the pairing symmetry of $(\mathrm{K,Tl})\mathrm{Fe}_x\mathrm{Se}_2$ compounds. We close by noting that recent experiments have suggested coexistence of a large moment antiferromagnetic order and superconductivity [13] or a phase separation [35]. Theoretically, how superconducting and magnetic orders interplay in these materials is an intriguing question for future studies.

This work was supported by NSF Grant No. DMR-1006985 and the Robert A. Welch Foundation Grant No. C-1411 (R.Y., P.G. and Q.S.), and U.S. DOE at LANL under Contract No. DE-AC52-06NA25396 (J.-X.Z.).

---

[*] Contributed equally to this work.

[1] J. Guo *et al.*, Phys. Rev. B **82**, 180520 (2010).
[2] M. Fang *et al.*, arxiv:1012.5236.
[3] A. Krzton-Maziopa *et al.*, J. Phys.: Condens. Matter **23**, 052203 (2011).
[4] Y. Mizuguchi *et al.*, Appl. Phys. Lett. **98**, 042511 (2011).
[5] Y. Zhang *et al.*, arxiv:1012.5980.
[6] T. Qian *et al.*, arxiv:1101.4923.
[7] D. Mou *et al.*, Phys. Rev. Lett. **106**, 107001 (2011).
[8] I. R. Shein and A. L. Ivanovskii, arXiv:1012.5164.
[9] X-W Yan *et al.*, arxiv:1012.5536.
[10] C. Cao and J. Dai, arxiv:1012.5621.
[11] L. Zhang and D. J. Singh, Phys. Rev. B **79**, 094528 (2009).
[12] D. M. Wang *et al.*, arxiv:1101.0789.
[13] W. Bao *et al.*, arxiv:1102.0830
[14] R. Yu, J-X. Zhu, and Q. Si, arxiv:1101.3307
[15] Y. Zhou *et al.*, arxiv:1101.4462.
[16] J.-X. Zhu *et al.*, Phys. Rev. Lett. **104**, 216405 (2010).
[17] M. Qazilbash *et al.*, Nat. Phys. **5**, 647 (2009).
[18] W. Z. Hu *et al.*, Phys. Rev. Lett. **101**, 257005 (2008).
[19] A. V. Boris *et al.*, Phys. Rev. Lett. **102**, 027001 (2009).
[20] J. Yang *et al.*, Phys. Rev. Lett. **102**, 027001 (20009).
[21] Q. Si, and E. Abrahams, Phys. Rev. Lett. **101**, 076401 (2008).
[22] J. Dai *et al.*, PNAS **106**, 4118 (2009); Q. Si *et al.*, New J. Phys. **11**, 045001 (2009).
[23] A. Kutepov *et al.*, Phys. Rev. B **82**, 045105 (2010).
[24] Z. G. Chen *et al.*, arxiv:1101.0572.
[25] K. Seo, B. A. Bernevig, and J. P. Hu, Phys. Rev. Lett. **101**, 206404 (2008).
[26] W. Q. Chen *et al.*, Phys. Rev. Lett. **102**, 047006 (2009).
[27] P. Goswami, P. Nikolic, and Q. Si, EPL **91**, 37006 (2010).
[28] A. Moreo *et al.*, Phys. Rev. B **79**, 134502 (2009).
[29] E. Berg, S. A. Kivelson, and D. J. Scalapino, arXiv:0905.1096.
[30] R. Thomale *et al.*, arxiv:1101.3593.
[31] F. Wang, *et al.*, arxiv:1101.4399.
[32] T. A. Maier *et al.*, arxiv:1101.4988.
[33] T. Das and A. V. Balatsky, arXiv:1101.6056.
[34] EPAPS Document No. X-XXX-XXXXXX-XXX-XXXXXX;see Supplementary Material for details.
[35] Z. Wang *et al.*, arxiv:1101.2059.
[36] F. Han *et al.*, arxiv:1103.1347.
[37] G. Kotliar, Phys. Rev. B **37**, 3664 (1988).
[38] S. Graser *et al.*, New J. Phys. **11**, 025016 (2009).
[39] S. Raghu *et al.*, Phys. Rev. B **77**, 220503 (2008).

SUPPLEMENTARY MATERIAL FOR EPAPS

I. DETAILS OF TIGHT-BINDING PARAMETRIZATION

For the five orbital, tetragonal symmetry preserving tight binding model, we adopt the parametrization of Ref.38. We have fitted the LDA band structure with the band dispersion found from the tight-binding model, to determine the hopping parameters. For iron pnictides we use the tight binding parameters of Ref.38. For $(\mathrm{K}, \mathrm{Tl})\mathrm{Fe}_x\mathrm{Se}_2$, we have performed calculations with two different sets of hopping parameters. These two sets respectively were derived from fitting the LDA results for $\mathrm{KFe_2Se_2}$, and $\mathrm{TlFe_2Se_2}$. In the main text we have shown the electron pockets and pairing phase diagram for the band structure corresponding to $\mathrm{KFe}_x\mathrm{Se}_2$. In this section we provide the explicit parametrization and band dispersions for both tight-binding models, and also show the electron pockets derived from $\mathrm{TlFe_2Se_2}$.

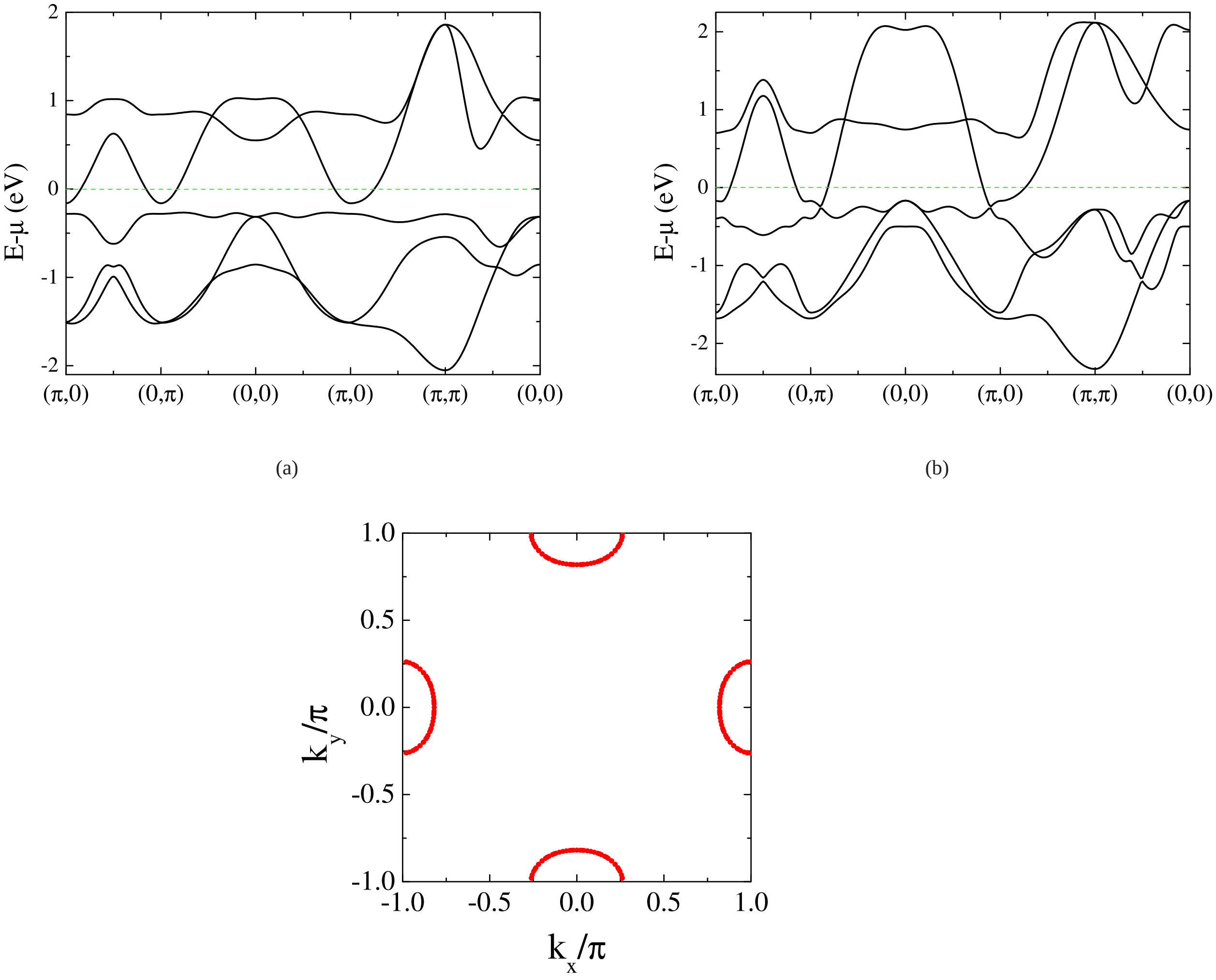

(a)

(b)

(c)

FIG. 5. The band dispersions of (a) $\mathrm{KFe_2Se_2}$ and (b) $\mathrm{TlFe_2Se_2}$, along the high-symmetry directions of the extended Brillouin zone (one iron/ unit cell). The band dispersions have been obtained by diagonalizing the appropriate five orbital tight binding model. In panel (c) we show the Fermi surfaces of $\mathrm{TlFe}_x\mathrm{Se}_2$ with electron doping $\delta = 0.15$, which consist of only electron pockets at M points.

Tight-binding model for $\mathbf{KFe_2Se_2}$*:* The following 5×5 tight binding matrix $\hat{\xi}_k$ for $\mathrm{KFe}_x\mathrm{Se}_2$ has been used. The orbital indices 1, 2, 3, 4 and 5 respectively correspond to d_{xz}, d_{yz}, $d_{x^2-y^2}$, d_{xy}, and $d_{3z^2-r^2}$ orbitals.

$$\begin{aligned}
\xi_{\mathbf{k}}^{11} &= -0.36559 - 0.1095\cos k_x - 0.81736\cos k_y + 0.83524\cos k_x\cos k_y + 0.03114(\cos 2k_x - \cos 2k_y)\\
&\quad -0.03464\cos 2k_x\cos k_y - 0.12572\cos 2k_y\cos k_x + 0.07596\cos 2k_x\cos 2k_y\\
\xi_{\mathbf{k}}^{22} &= -0.36559 - 0.81736\cos k_x - 0.1095\cos k_y + 0.83524\cos k_x\cos k_y - 0.03114(\cos 2k_x - \cos 2k_y)\\
&\quad -0.12572\cos 2k_x\cos k_y - 0.03464\cos 2k_y\cos k_x + 0.07596\cos 2k_x\cos 2k_y\\
\xi_{\mathbf{k}}^{33} &= -0.56466 + 0.65046(\cos k_x + \cos k_y) - 0.39132\cos k_x\cos k_y - 0.01074(\cos 2k_x + \cos 2k_y)\\
\xi_{\mathbf{k}}^{44} &= -0.00096 + 0.41266(\cos k_x + \cos k_y) + 0.26328\cos k_x\cos k_y - 0.0705(\cos 2k_x + \cos 2k_y)\\
&\quad -0.08756(\cos 2k_x\cos k_y + \cos 2k_y\cos k_x) + 0.01692\cos 2k_x\cos 2k_y\\
\xi_{\mathbf{k}}^{55} &= -0.91583 - 0.0854(\cos k_x + \cos k_y) + 0.02234(\cos 2k_x + \cos 2k_y)\\
&\quad +0.00708(\cos 2k_x\cos k_y + \cos 2k_y\cos k_x) - 0.05396\cos 2k_x\cos 2k_y\\
\xi_{\mathbf{k}}^{12} &= -0.40644\sin k_x\sin k_y + 0.08068(\sin 2k_x\sin k_y + \sin 2k_y\sin k_x) - 0.13092\sin 2k_x\sin 2k_y = \xi_{\mathbf{k}}^{21*}\\
\xi_{\mathbf{k}}^{13} &= -0.62894i\sin k_y + 0.249i\sin k_y\cos k_x - 0.0412i(\sin 2k_y\cos k_x - \cos 2k_x\sin k_y) = \xi_{\mathbf{k}}^{31*}\\
\xi_{\mathbf{k}}^{23} &= 0.62894i\sin k_x - 0.249i\sin k_x\cos k_y + 0.0412i(\sin 2k_x\cos k_y - \cos 2k_y\sin k_x) = \xi_{\mathbf{k}}^{32*}\\
\xi_{\mathbf{k}}^{14} &= 0.2757i\sin k_x + 0.0042i\cos k_y\sin k_x + 0.0416i\sin 2k_x\cos k_y = \xi_{\mathbf{k}}^{41*}\\
\xi_{\mathbf{k}}^{24} &= 0.2757i\sin k_y + 0.0042i\cos k_x\sin k_y + 0.0416i\sin 2k_y\cos k_x = \xi_{\mathbf{k}}^{42*}\\
\xi_{\mathbf{k}}^{15} &= -0.0965i\sin k_y + 0.40384i\sin k_y\cos k_x + i(0.04816)\sin 2k_y\cos 2k_x = \xi_{\mathbf{k}}^{51*}\\
\xi_{\mathbf{k}}^{25} &= -0.0965i\sin k_x + 0.40384i\sin k_x\cos k_y + 0.04816i\sin 2k_x\cos 2k_y = \xi_{\mathbf{k}}^{52*}\\
\xi_{\mathbf{k}}^{34} &= -0.1918(\sin 2k_y\sin k_x - \sin 2k_x\sin k_y) = \xi_{\mathbf{k}}^{43}\\
\xi_{\mathbf{k}}^{35} &= -0.61932(\cos k_x - \cos k_y) - 0.05992(\cos 2k_x\cos k_y - \cos 2k_y\cos k_x) = \xi_{\mathbf{k}}^{53}\\
\xi_{\mathbf{k}}^{45} &= -0.33436\sin k_x\sin k_y - 0.03064\sin 2k_x\sin 2k_y = \xi_{\mathbf{k}}^{54}
\end{aligned} \tag{4}$$

$\mathbf{TlFe_2Se_2}$ *:* The following 5×5 tight binding matrix $\hat{\xi}_k$ has been deriving from fitting the LDA results of $\mathrm{TlFe_2Se_2}$.

$$\begin{aligned}
\xi_{\mathbf{k}}^{11} &= -0.35956 - 0.48396\cos k_x - 0.69426\cos k_y + 0.93156\cos k_x\cos k_y + 0.20428(\cos 2k_x - \cos 2k_y)\\
&\quad -0.23556\cos 2k_x\cos k_y + 0.2714\cos 2k_y\cos k_x + 0.02912\cos 2k_x\cos 2k_y\\
\xi_{\mathbf{k}}^{22} &= -0.35956 - 0.69426\cos k_x - 0.48396\cos k_y + 0.93156\cos k_x\cos k_y - 0.20428(\cos 2k_x - \cos 2k_y)\\
&\quad +0.2714\cos 2k_x\cos k_y - 0.23556\cos 2k_y\cos k_x + 0.02912\cos 2k_x\cos 2k_y\\
\xi_{\mathbf{k}}^{33} &= -1.11574 + 0.76802(\cos k_x + \cos k_y) - 0.10188\cos k_x\cos k_y + 0.02612(\cos 2k_x + \cos 2k_y)\\
\xi_{\mathbf{k}}^{44} &= 0.09324 + 0.76338(\cos k_x + \cos k_y) + 0.63348\cos k_x\cos k_y - 0.06164(\cos 2k_x + \cos 2k_y)\\
&\quad -0.18652(\cos 2k_x\cos k_y + \cos 2k_y\cos k_x) - 0.1074\cos 2k_x\cos 2k_y\\
\xi_{\mathbf{k}}^{55} &= -0.74545 + 0.07376(\cos k_x + \cos k_y) - 0.05124(\cos 2k_x + \cos 2k_y)\\
&\quad -0.12872(\cos 2k_x\cos k_y + \cos 2k_y\cos k_x) + 0.08408\cos 2k_x\cos 2k_y\\
\xi_{\mathbf{k}}^{12} &= -0.97632\sin k_x\sin k_y - 0.01744(\sin 2k_x\sin k_y + \sin 2k_y\sin k_x) - 0.04692\sin 2k_x\sin 2k_y = \xi_{\mathbf{k}}^{21*}\\
\xi_{\mathbf{k}}^{13} &= -0.73408i\sin k_y - 0.08848i\sin k_y\cos k_x + 0.10508i(\sin 2k_y\cos k_x - \cos 2k_x\sin k_y) = \xi_{\mathbf{k}}^{31*}\\
\xi_{\mathbf{k}}^{23} &= 0.73408i\sin k_x + 0.08848i\sin k_x\cos k_y - 0.10508i(\sin 2k_x\cos k_y - \cos 2k_y\sin k_x) = \xi_{\mathbf{k}}^{32*}\\
\xi_{\mathbf{k}}^{14} &= 0.46354i\sin k_x - 0.22408i\cos k_y\sin k_x + 0.15492i\sin 2k_x\cos k_y = \xi_{\mathbf{k}}^{41*}\\
\xi_{\mathbf{k}}^{24} &= 0.46354i\sin k_y - 0.22408i\cos k_x\sin k_y + 0.15492i\sin 2k_y\cos k_x = \xi_{\mathbf{k}}^{42*}\\
\xi_{\mathbf{k}}^{15} &= -0.26344i\sin k_y + 0.24328i\sin k_y\cos k_x - 0.11724i\sin 2k_y\cos 2k_x = \xi_{\mathbf{k}}^{51*}\\
\xi_{\mathbf{k}}^{25} &= -0.26344i\sin k_x + 0.24328i\sin k_x\cos k_y - 0.11724i\sin 2k_x\cos 2k_y = \xi_{\mathbf{k}}^{52*}\\
\xi_{\mathbf{k}}^{34} &= -0.20372(\sin 2k_y\sin k_x - \sin 2k_x\sin k_y) = \xi_{\mathbf{k}}^{43}\\
\xi_{\mathbf{k}}^{35} &= -0.4617(\cos k_x - \cos k_y) + 0.13144(\cos 2k_x\cos k_y - \cos 2k_y\cos k_x) = \xi_{\mathbf{k}}^{53}\\
\xi_{\mathbf{k}}^{45} &= -0.6828\sin k_x\sin k_y - 0.1088\sin 2k_x\sin 2k_y = \xi_{\mathbf{k}}^{54}
\end{aligned} \tag{5}$$

II. PAIRING AMPLITUDES FOR $\mathrm{TlFe_xSe_2}$ AND IRON PNICTIDES

In this section we first show the pairing phase diagram $\mathrm{TlFe}_x\mathrm{Se}_2$ in Fig. 6(a), for electron doping $\delta = 0.15$. Also shown, Fig. 6(b), are the dominant pairing amplitudes projected onto the xz/yz 3d-orbitals. The phase diagram and the strength of the pairing amplitudes are similar to those of $\mathrm{KFe}_x\mathrm{Se}_2$, described in the main text. In Fig. 7(a) and Fig. 7(b), we respectively show three dimensional plots of the pairing amplitudes for $\mathrm{TlFe}_x\mathrm{Se}_2$ and iron pnictides, both with an electron doping $\delta = 0.15$.

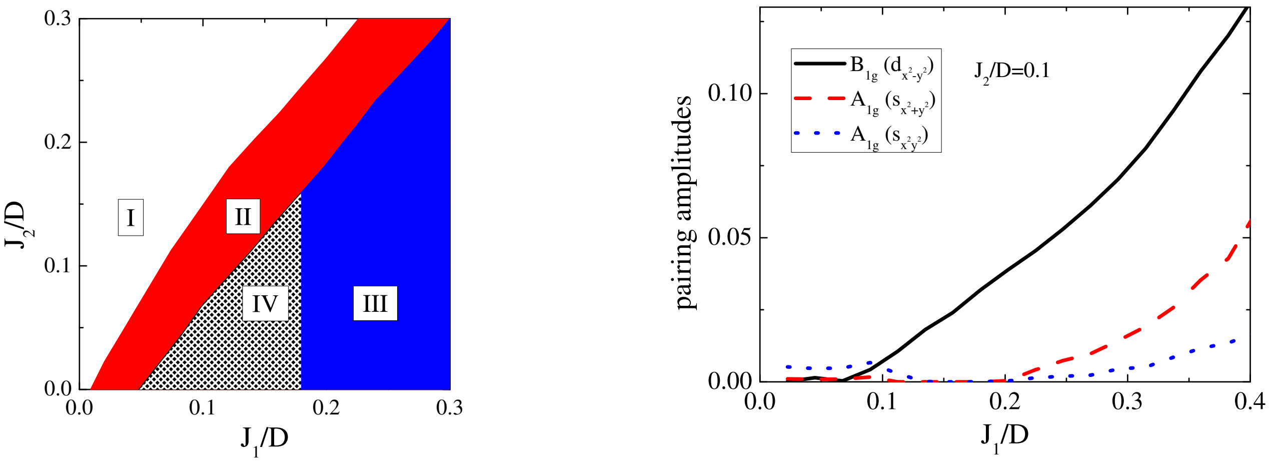

(a) (b)

FIG. 6. In panel (a) we show the zero temperature phase diagram of $\mathrm{TlFe}_x\mathrm{Se}_2$ for an electron doping $\delta = 0.15$. The phase diagram is similar to that of $\mathrm{KFe}_x\mathrm{Se}_2$ (Fig. 2(a)). The regions I, II, III, and IV respectively correspond to an A_{1g} state with $s_{x^2y^2}$ as the dominant pairing channel, a time reversal symmetry breaking $\mathrm{A}_{1g}+i\mathrm{B}_{1g}$ state with $s_{x^2y^2}$ and $d_{x^2-y^2}$ as the dominant A_{1g} and B_{1g} pairing channels, a likewise $\mathrm{A}_{1g}+i\mathrm{B}_{1g}$ state with $s_{x^2+y^2}$ and $d_{x^2-y^2}$ as the dominant A_{1g} and B_{1g} pairing channels, and a pure B_{1g} state with $d_{x^2-y^2}$ pairing channel. In panel (b) we show the competing dominant pairing amplitudes A_{1g} $s_{x^2y^2}$, A_{1g} $s_{x^2+y^2}$, B_{1g} $s_{x^2y^2}$ for xz/d_{yz} orbitals of $\mathrm{TlFe}_x\mathrm{Se}_2$ with an electron doping $\delta = 0.15$, and $\mathrm{J}_2/\mathrm{D} = 0.1$.

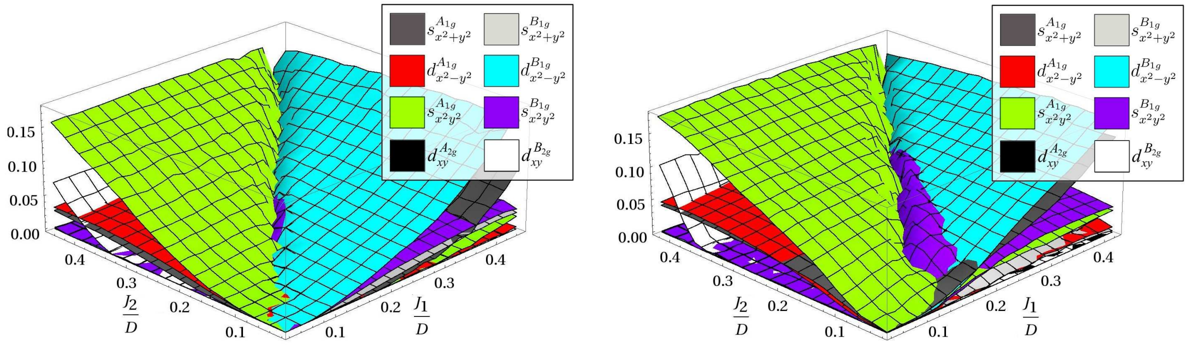

(a) (b)

FIG. 7. The pairing amplitudes for xz/yz orbitals of (a) $\mathrm{TlFe}_x\mathrm{Se}_2$ and (b) iron pnictides with electron doping $\delta = 0.15$. Compared to $\mathrm{TlFe}_x\mathrm{Se}_2$, iron pnictides have stronger A_{1g} $s_{x^2+y^2}$ pairing.

III. PAIRING PHASE DIAGRAMS OF A TWO ORBITAL MODEL WITH AND WITHOUT DOPING DEPENDENT BAND RENORMALIZATION

To demonstrate the robustness of our pairing phase diagram against the doping dependent band renormalization effects, we consider a two orbital model involving only xz and yz orbitals. For simplicity we consider hole doping; the electron doping case can be treated in a similar manner after performing a particle-hole transformation. The Hamiltonian of interest is

$$H=-\sum_{i<j,\alpha,\beta,\sigma} t_{ij}^{\alpha\beta} c_{i\alpha\sigma}^{\dagger} c_{j\beta\sigma}+h.c.-\mu \sum_{i,\alpha,\sigma} c_{i\alpha\sigma}^{\dagger} c_{i\alpha\sigma}+\sum_{i<j,\alpha,\beta} J_{ij}^{\alpha\beta}\left(\vec{S}_{i\alpha}\cdot\vec{S}_{j\beta}-\frac{1}{4} n_{i\alpha} n_{j\beta}\right) \tag{6}$$

with the double occupancy prohibiting constraint $\sum_{\sigma} c_{i\alpha\sigma}^{\dagger} c_{i\alpha\sigma} \leq 1$ for each orbital. The constraint is imposed by introducing slave boson operator b_i and fermionic spinon operator f_i for each orbital [37] and the Hamiltonian is transformed to

$$\begin{aligned} H= & -\sum_{i<j,\alpha,\beta,\sigma} t_{ij}^{\alpha\beta} f_{i\alpha\sigma}^{\dagger} b_{i\alpha} b_{j\beta}^{\dagger} f_{j\beta\sigma}+h.c.-\mu \sum_{i,\alpha,\sigma} f_{i\alpha\sigma}^{\dagger} f_{i\beta\sigma}-\sum_{i<j,\alpha,\beta} \frac{J_{ij}^{\alpha\beta}}{2} B_{ij,\alpha\beta}^{\dagger} B_{ij,\alpha\beta} \\ & +\sum_{i,\alpha} \lambda_{i\alpha}\left(\sum_{\sigma} f_{i\alpha\sigma}^{\dagger} f_{i\alpha\sigma}+b_{i\alpha}^{\dagger} b_{i\alpha}-1\right) \end{aligned} \tag{7}$$

where $B_{ij,\alpha\beta}^{\dagger}=(f_{i\alpha\uparrow}^{\dagger} f_{j\beta\downarrow}^{\dagger}-f_{i\alpha\downarrow}^{\dagger} f_{j\beta\uparrow}^{\dagger})$ is the spin-singlet pairing operator for the fermionic spinons, and $\lambda_{i,\alpha}$'s are Lagnrage multipliers which enforce the occupancy constraints. At zero temperature the slave bosons are bose condensed and the bose operators have finite expectation values. In the tetragonal symmetry breaking particle-hole channel order, we have $\langle b_{i,1}\rangle = \langle b_{i,2}\rangle = \sqrt{\delta/2}$, where δ is the hole doping and $\langle\lambda_{i,1}\rangle = \langle\lambda_{i,2}\rangle = \lambda$, which is absorbed into the chemical potential. The expectation value of the bose operators renormalizes the kinetic energy term by a factor of $\delta/2$. As in the main text we choose the interactions to be diagonal in the orbital space. After mean-field decoupling, the free energy density

$$f=\frac{J_1}{2}\sum_{\alpha}(|\Delta_{x,\alpha\alpha}|^2+|\Delta_{y,\alpha\alpha}|^2)+\frac{J_2}{2}\sum_{\alpha}(|\Delta_{x+y,\alpha\alpha}|^2+|\Delta_{x-y,\alpha\alpha}|^2)-\int\frac{d^2k}{4\pi^2}(\mathcal{E}_{\mathbf{k}+}+\mathcal{E}_{\mathbf{k}-}-\frac{\delta}{2}E_{\mathbf{k}+}-\frac{\delta}{2}E_{\mathbf{k}-}+2\mu) \tag{8}$$

is minimized with respect to pairing amplitudes with the constraint $n_1=n_2=1-\frac{\delta}{2}$. The quasiparticle dispersions $\mathcal{E}_{\mathbf{k}\pm}$ in the paired state are calculated from the 4×4 Nambu matrix

$$\hat{h}_{\mathbf{k}}=\begin{bmatrix} \frac{\delta\hat{\xi}_{\mathbf{k}}}{2}-\mu\mathbb{1}_{2\times 2} & \boldsymbol{\Delta}_{\mathbf{k}} \\ \boldsymbol{\Delta}_{\mathbf{k}}^{*} & -\frac{\delta\hat{\xi}_{\mathbf{k}}}{2}+\mu\mathbb{1}_{2\times 2} \end{bmatrix} \tag{9}$$

where

$$\tilde{\Delta}_{\mathbf{k},\alpha\alpha}=J_1\left(\Delta_{x,\alpha\alpha}\cos(k_x)+\Delta_{y,\alpha\alpha}\cos(k_y)\right)+J_2\left(\Delta_{x+y,\alpha\alpha}\cos(k_x+k_y)+\Delta_{x-y,\alpha\alpha}\cos(k_x-k_y)\right) \tag{10}$$

For the band structure we choose the two orbital tight-binding model of Ref. 39. The 2×2 tight-binding matrix $\hat{\xi}_{\mathbf{k}}=\hat{\xi}_{\mathbf{k}}=\xi_{\mathbf{k}+}\mathbb{1}_{2\times 2}+\xi_{\mathbf{k}-}\tau_z+\xi_{\mathbf{k}xy}\tau_x$, where Pauli matrices τ_i) operate on the orbital indices, and $\xi_{\mathbf{k}+}=-(t_1+t_2)(\cos k_x+\cos k_y)-4t_3\cos k_x\cos k_y$, $\xi_{\mathbf{k}-}=-(t_1-t_2)(\cos k_x-\cos k_y)$, $\xi_{\mathbf{k}xy}=-4t_4\sin k_x\sin k_y$ are respectively A_{1g}, B_{1g} and B_{2g} functions. The band dispersion relations $E_{\mathbf{k}\pm}=\xi_{\mathbf{k}+}\pm\sqrt{\xi_{\mathbf{k}-}^2+\xi_{\mathbf{k}xy}^2}$, give rise to two electron pockets at $\mathbf{k}=(\pi,0)$ and $(0,\pi)$, and two hole pockets at $\mathbf{k}=(0,0)$ and (π,π). The following values of the hopping parameters, $t_1=-t$, $t_2=1.3t$, $t_3=t_4=-0.85t$ were obtained in Ref. 39, by a fitting of the LDA bands. The quasiparticle dispersions in the paired state are given by

$$\begin{aligned} \mathcal{E}_{\mathbf{k}\pm}= & \left[\left(\left(\frac{\delta\xi_{\mathbf{k}+}}{2}-\mu\right)^2+\frac{\delta^2}{4}\left(\xi_{\mathbf{k}-}^2+\xi_{\mathbf{k}xy}^2\right)+\frac{|\tilde{\Delta}_{\mathbf{k},11}|^2}{2}+\frac{|\tilde{\Delta}_{\mathbf{k},22}|^2}{2}\right)\pm\left\{\left(\delta\xi_{\mathbf{k}-}\left(\frac{\delta\xi_{\mathbf{k}+}}{2}-\mu\right)\right.\right.\right. \\ & \left.\left.\left.+\frac{|\tilde{\Delta}_{\mathbf{k},11}|^2}{2}-\frac{|\tilde{\Delta}_{\mathbf{k},22}|^2}{2}\right)^2+\delta^2\xi_{\mathbf{k}xy}^2\left(\left(\frac{\delta\xi_{\mathbf{k}+}}{2}-\mu\right)^2+\frac{1}{4}|\tilde{\Delta}_{\mathbf{k},11}-\tilde{\Delta}_{\mathbf{k},22}|^2\right)\right\}^{\frac{1}{2}}\right]^{\frac{1}{2}} \end{aligned} \tag{11}$$

After explicitly accounting for the occupancy constraints and associated band renormalization we obtain the pairing phase diagram shown in Fig. 8(a). A qualitatively similar phase diagram for this model, obtained by ignoring the band renormalization effects, is shown in Fig. 8(b).

IV. ORBITAL CHARACTER OF THE FERMI SURFACE AND PAIRING AMPLITUDES FOR xy ORBITAL

In this section we first show the orbital weights on the electron pockets for both $\mathrm{KFe}_x\mathrm{Se}_2$ and pnictides, for electron doping $\delta=0.15$ respectively in Fig. 9(a) and Fig. 9(b). For pnictides, the xz/yz orbitals have the dominant orbital weights on the

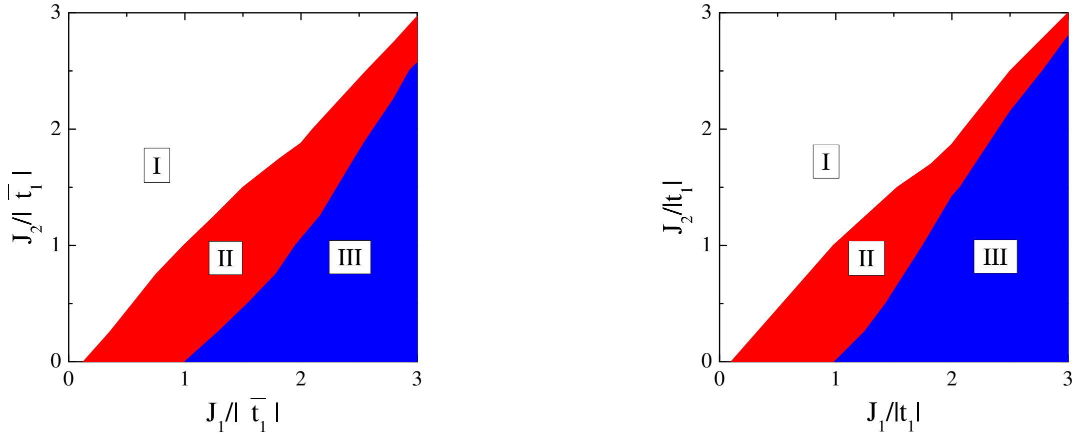

(a)

(b)

FIG. 8. Qualitatively similar zero temperature phase diagrams of a two orbital $\mathrm{t}-\mathrm{J}_1-\mathrm{J}_2$ model obtained (a) by considering a doping dependent renormalization of the band dispersions due to the local constraint of zero double occupancies and (b) by ignoring the doping dependent band renormalization. In (a) the effective hopping parameters $\bar{t}_i = t_i\frac{\delta}{2}$. The regions I, II, and III respectively correspond to an A_{1g} state with $s_{x^2y^2}$ as the dominant pairing channel, a time reversal symmetry breaking $\mathrm{A}_{1g} + i\mathrm{B}_{1g}$ state with $s_{x^2y^2}$ and $d_{x^2-y^2}$ as the dominant A_{1g} and B_{1g} pairing channels, and a likewise $\mathrm{A}_{1g} + i\mathrm{B}_{1g}$ state with $s_{x^2+y^2}$ and $d_{x^2-y^2}$ as the dominant A_{1g} and B_{1g} pairing channels.

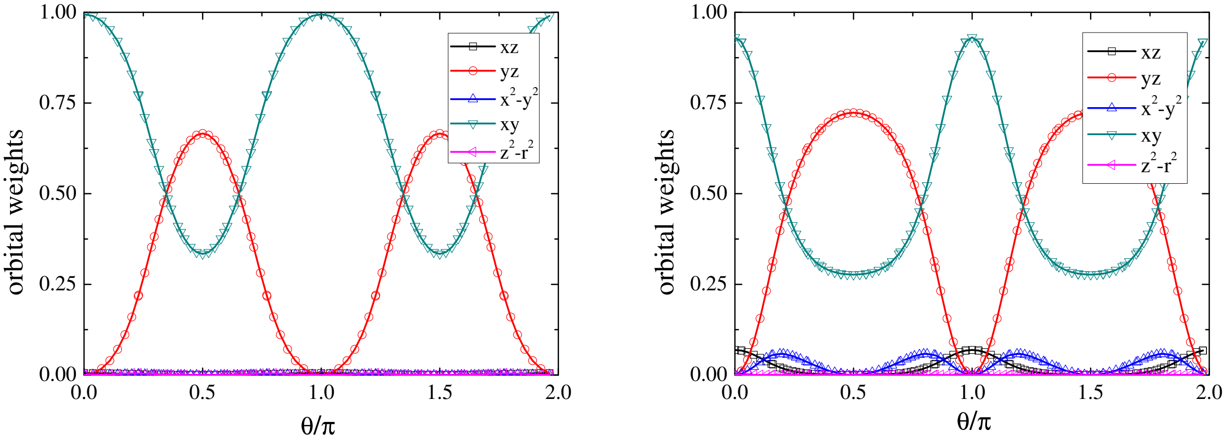

(a)

(b)

FIG. 9. The orbital weights on the electron pocket centered at $(\pi, 0)$ of (a) $\mathrm{KFe}_x\mathrm{Se}_2$ and (b) iron pnictides for electron doping $\delta = 0.15$. θ is the winding angle of the pocket with respect to its center. The weights on the electron pocket centered at $(0, \pi)$ can be obtained by interchanging the xz and yz components and shifting θ by $\pi/2$.

two hole pockets (not shown), and also contribute significantly on the electron pockets. Whereas for $\mathrm{KFe}_x\mathrm{Se}_2$ (and also for $\mathrm{TlFe}_x\mathrm{Se}_2$), there are no hole pockets, and the contribution from xy orbital is considerably enhanced on the electron pockets. This indicates that the xy orbital plays a more important role in building the electron pocket of $(\mathrm{K},\mathrm{Tl})\mathrm{Fe}_x\mathrm{Se}_2$ than in pnictides.

The enhanced xy orbital character on Fermi surface of $\mathrm{KFe}_x\mathrm{Se}_2$ affects the electron pairing. To see this we show the pairing amplitudes at $J_2/D = 0.1$ of xy orbital for both $\mathrm{KFe}_x\mathrm{Se}_2$ and pnictides at electron doping $\delta = 0.15$ in Fig. 10(a) and Fig. 10(b), respectively. Comparing with Fig. 4(a) and Fig. 4(b) we see that for pnictides, the contribution to the three competing dominant pairings from the xz/yz orbital is comparable with the one from xy orbital. But for $\mathrm{KFe}_x\mathrm{Se}_2$, the contribution from xy orbital can be stronger. This is especially true in the regime $J_1/D \lesssim 0.07$, where only A_{1g} pairing is present.

Overall, however, the pairing amplitudes for the xy orbital are similar between $(\mathrm{K},\mathrm{Tl})\mathrm{Fe}_x\mathrm{Se}_2$ and iron pnictides. This is seen in the three-dimensional plots given in Figs. 11(a) and 11(b), which are similar to their counterparts for the xz/yz orbitals (Figs. 3 and 7(b)).

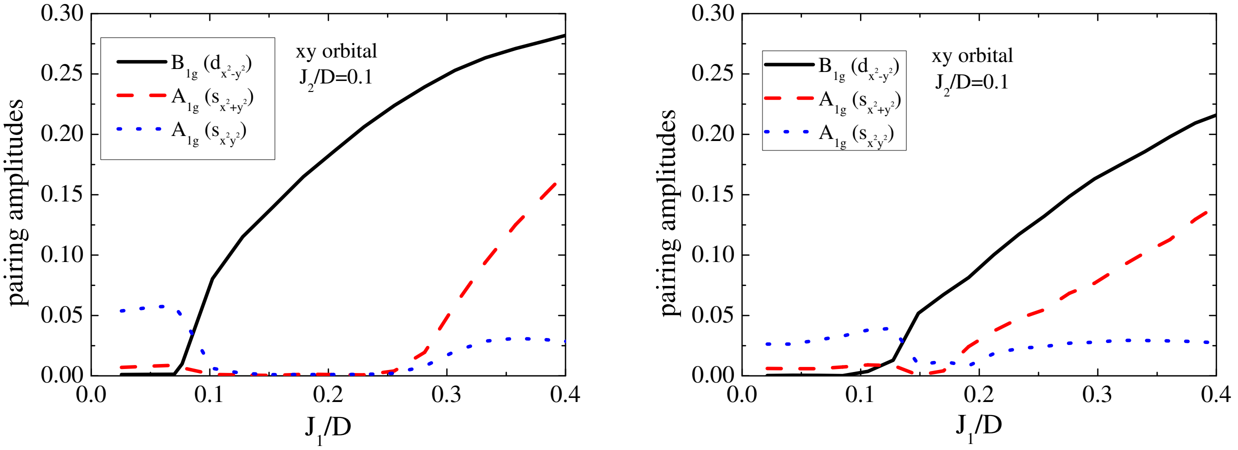

(a)

(b)

FIG. 10. The competing dominant pairing amplitudes A_{1g} $\mathrm{s}_{x^2y^2}$, A_{1g} $\mathrm{s}_{x^2+y^2}$, B_{1g} $\mathrm{d}_{x^2-y^2}$ at $J_2/D = 0.1$ of d_{xy} orbital for (a) $\mathrm{KFe}_x\mathrm{Se}_2$ and (b) iron pnictides for electron doping $\delta = 0.15$.

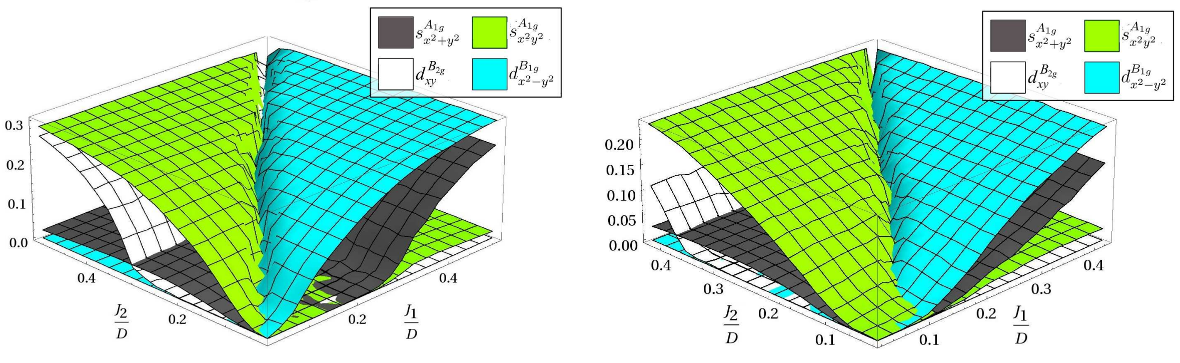

(a)

(b)

FIG. 11. The pairing amplitudes for the xy orbital of (a) $\mathrm{KFe}_x\mathrm{Se}_2$ and (b) iron pnictides, both for electron doping $\delta = 0.15$.